



## 3D ultrasound computer tomography: Hardware setup, reconstruction methods and first clinical results



Hartmut Gemmeke<sup>a,\*</sup>, Torsten Hopp<sup>a</sup>, Michael Zapf<sup>a</sup>, Clemens Kaiser<sup>b</sup>, Nicole V. Ruiter<sup>a</sup>

<sup>a</sup> Karlsruhe Institute of Technology (KIT), Institute for Data Processing and Electronics, Karlsruhe, Germany

<sup>b</sup> University Medical Center, Mannheim, Germany

### ARTICLE INFO

#### Article history:

Received 30 November 2016

Received in revised form

21 June 2017

Accepted 11 July 2017

Available online 27 July 2017

#### Keywords:

Ultrasound computer tomography

3D synthetic aperture focusing technique

In-vivo images

### ABSTRACT

A promising candidate for improved imaging of breast cancer is ultrasound computer tomography (USCT). Current experimental USCT systems are still focused in elevation dimension resulting in a large slice thickness, limited depth of field, loss of out-of-plane reflections, and a large number of movement steps to acquire a stack of images. 3D USCT emitting and receiving spherical wave fronts overcomes these limitations. We built an optimized 3D USCT, realizing for the first time the full benefits of a 3D system. The point spread function could be shown to be nearly isotropic in 3D, to have very low spatial variability and fit the predicted values. The contrast of the phantom images is very satisfactory in spite of imaging with a sparse aperture. The resolution and imaged details of the reflectivity reconstruction are comparable to a 3 T MRI volume. Important for the obtained resolution are the simultaneously obtained results of the transmission tomography. The KIT 3D USCT was then tested in a pilot study on ten patients. The primary goals of the pilot study were to test the USCT device, the data acquisition protocols, the image reconstruction methods and the image fusion techniques in a clinical environment. The study was conducted successfully; the data acquisition could be carried out for all patients with an average imaging time of six minutes per breast. The reconstructions provide promising images. Overlaid volumes of the modalities show qualitative and quantitative information at a glance. This paper gives a summary of the involved techniques, methods, and first results.

© 2017 Elsevier B.V. All rights reserved.

### 1. Introduction

Ultrasound computer tomography (USCT) was first investigated in the 1970s, e.g. the work by Schomberg [1]. The main advantages of such USCT systems for breast cancer detection and diagnosis are simultaneously recordings of reflection, attenuation and speed of sound images, high image quality, fast data acquisition, and no use of ionization radiation.

Building such a device for clinical practice was not successful for a long time - mostly due to the huge data rate and the time-consuming image reconstruction. Yet, promising ex-vivo results have been archived by numerous groups, e.g. [2–5]. Currently, the first 2D and 2.5D systems have become available for clinical evaluation [6,7]. Usually USCT systems implement unfocused ultrasound emission and reception to reconstruct optimally focused reflection images by synthetic aperture post-beamforming. However, in most systems post-beamforming is only applied in one imaging plane. This leads to large slice thickness with limited

depth of field, loss of out-of-plane reflections, and large number of movement steps to acquire a stack of images of the whole volume [7]. 3D USCT, using spherical wave fronts for imaging, overcomes these limitations [8].

However, a 3D system requires a large number of transducers approx. two orders of magnitude larger than in a 2D system to fulfil the sampling theorem. In order to approximate a spherical wave front, the individual transducer area has to be small, which leads to low sound pressure and lower signal-to-noise ratio (SNR). For in-vivo imaging, the data acquisition time has to be short to prevent image degradation by patient movement. Also, the image reconstruction using post-beamforming is very time consuming.

The aims of our work gathered in this paper are

1. to provide a summary of the KIT 3D USCT II, the first full 3D system for in-vivo imaging,
2. to demonstrate, that with a sparse transducer setup it is possible to get a good resolution for diagnostics,
3. to show, that 3D acquisition and reconstruction of speed of sound and attenuation images give a direct access to tissue types and cancer detection as proposed by Greenleaf [9] and

\* Corresponding author.

E-mail address: [hartmut.gemmeke@kit.edu](mailto:hartmut.gemmeke@kit.edu) (H. Gemmeke).

**Table 1**  
Specification of KIT 3D USCT.

Type of specification	Value
No. parallel channels	480
Digitization	20 MHz @ 12 bit
On-board memory	80 GByte
Multiplex factor	3
Averaging	1 to 128
No. TAS	157
No. emitters	628
No. receivers	1,413
Diameter TAS	28 mm
Emitters/TAS	4
Receivers/TAS	9
Receiver channels/TAS	3
Area individual transducer	(0.9 mm) <sup>2</sup>
No. sub-elements/transducer	2 × 2
Area sub-element	(0.4 mm) <sup>2</sup>
Max. excitation voltage	80
Opening angle	38, 2° ± 1.5°@ – 6 dB
Resonance frequency	2.5 ± 0.08 MHz
Bandwidth	1.5 ± 0.15 MHz@ – 6 dB
Sound pressure	5.9 ± 0.63 kPa@12 cm

4. to find the current limitations in our design resulting in an improved version now under construction for clinical application.

Our current prototype, the hardware setup, the image reconstruction methods and experimental and clinical results are described in this paper.

## 2. Methodology

The KIT 3D USCT is the world's first full 3D system aimed at in-vivo imaging. Therefore many methods had to be developed or adapted to build such an electronical and mechanical complex hardware and to develop the necessary software for readout and reconstruction, which will be described in this section.

### 2.1. Hardware setup

The KIT 3D USCT prototype is shown in Fig. 1. The patient is lying in a prone position on the patient bed. The breast is imaged in a fixed setup in a water bath. The aperture with 2041 transducers surrounds the breast. Due to no breast deformation and defined patient positioning, the volume images of the female breast are reproducible. The device has a semi-ellipsoidal aperture with 628 emitters and 1413 receivers. Approx. spherical wave fronts are generated by each emitter at 2.5 MHz (approx. 50% bandwidth). Rotational and translational movement, so-called aperture positions, of the complete sensor system creates further virtual positions of the ultrasound transducers. The aperture in form of a semi-ellipsoid was optimized in respect to the isotropy of the 3D point spread function (PSF), the image contrast and the illumination [8]. An overview of the specifications of the KIT 3D USCT is given in Table 1.

#### 2.1.1. Transducer array systems

Sound pressure is generated and received using lead-zirconate titanate (PZT) composites. One quadratic module of PZT composite contains nine receivers and four emitters. Each transducer array is embedded including its pre-amplifier and control electronics in the casing of the Transducer Array System (TAS).

The accuracy of the positioning of the transducers within the TAS is achieved by the production process: As matching layer of the transducers a thin Rogers TMM4 (ceramic thermoset polymer) board is employed, which contains the lower electrode for the PZT composites. (5.5 mm)<sup>2</sup> quadratic PZTs are glued to the matching layer using a pick-and-placer device. They are then diced by a wafer saw. The diced PZTs are contacted to the embedded electronics by wire bonding. The resulting transducer array consists of four emitters and nine receivers, each with a two by two structure of 400 µm times 400 µm sub-elements. The gap between the sub-elements is approx. 100 µm given by the width of the saw. The transducer array with attached electronics is then positioned within the TAS casing with an accuracy of 0.03 mm. Finally, the TAS is filled with polyurethane, which serves as waterproof filler and transducer backing.

For quality control, the variation of the sound pressure of 80 emitters in 20 arbitrarily chosen TAS have been measured over frequency and elevation angle using a hydrophone. The obtained resonance parameters and measured standard deviations are shown in Table 1.

Each TAS contains a temperature sensor for tracking the temperature distribution and shift at 157 positions during measurements. Additionally, two calibrated PT100 temperature sensors are embedded in the TAS holder to enable increased accuracy. The measured temperature distribution can be applied during the image reconstruction to estimate the distribution of the speed of sound in the contact medium water.

#### 2.1.2. Data acquisition hardware

The data acquisition is carried out with an FPGA based system, which can store up to 80 GByte of A-scans [10]. The system is housed in a 19" crate with a central processing board containing the control of the transducers, free programmable pulse shape of the transducer, and control of the system by a PCI Mezzanine Card (PMC) handling all input and output tasks of the crate. The PMC is a 1.4 GHz Pentium M board running Linux as operational system and supports a fast Ethernet interface and has a SATA interface to a solid-state drive for storage of the measured data.

The crate contains beside a central processing board acting as Bus master (SLT) 20 data acquisition boards (FLT) performing the analogue filtering and data acquisition. Each FLT contains 24 receiver channels, summing up to 480 channels processed simultaneously in the system and enabling data acquisition at one aperture position in approx. ten seconds. The digitalization is performed by three 8-fold (12 Bit @ 20 MHz) ADCs per board.

The analogue part of the FLT contains a differential receiver, programmable amplifier (variable over 20 dB), bandpass filter (0.5 to 4.6 MHz), and driver for the ADC. The oversampling frequency of 20 MHz is used to allow a lower (5th) order Nyquist filter. With enabled preamplifier and system filled with water the noise level is 2 LSB.

After digitization, the parallel data streams are processed by FPGAs. The data streams are bandpass filtered (1.67 to 3.33 MHz @ –60 dB) and the data rate is reduced by a factor of 6, performing bandpass under-sampling. Due to this down-sampling and 4-fold multiple sampling, the dynamic range could be enlarged to 16 bit. The reduced data is then stored in the internal memory buffer. Using this approach, it is possible to store up to 47 data sets at different aperture positions in one data acquisition process.

Each FLT provides 4 Altera Cyclone II EP2C35 FPGAs. One of these FPGAs is used as a controller (Ctrl-FPGA). It manages communication and data transfers to the other FPGAs on board and to the central control board. The remaining three FPGAs (Comp-FPGA) are dedicated to signal acquisition and data pre-processing. There are also two different types of memory modules as on-board storage: three static RAM modules (2 MB each) as

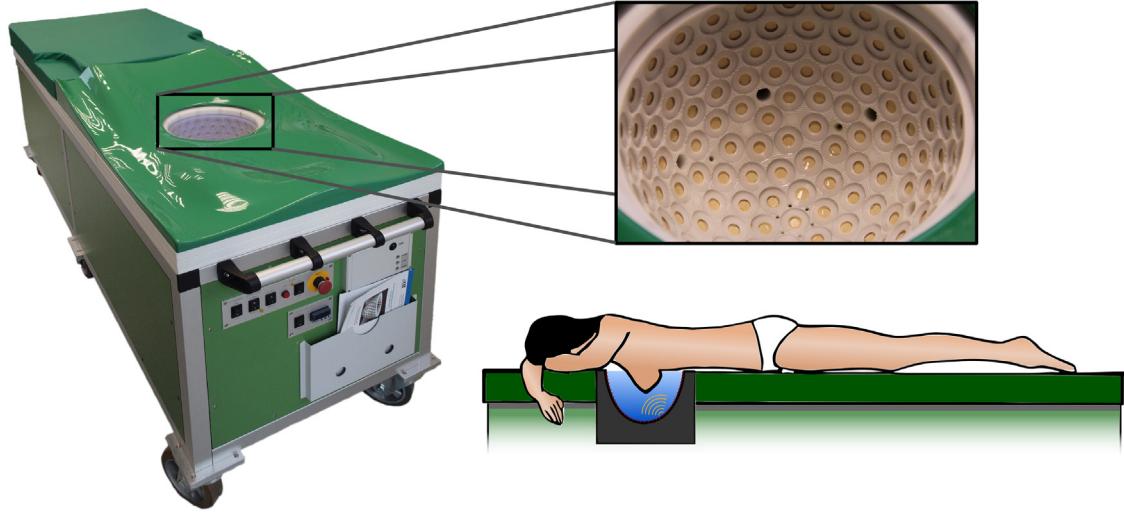


**Fig. 1.** Left: KIT 3D USCT patient bed. Top right: Detail view of US transducers forming the imaging aperture with 157 transducer array systems (TAS) containing 4 emitters and 9 receivers each. Bottom right: patient positioning on the patient bed during data acquisition. The breast is suspended freely in a warm water bath.

buffer memory and a larger dynamic RAM module (DDRII, 4 GB) as main storage element. Furthermore, there are two means of communication between the Cntrl-FPGA and the Comp-FPGAs on an FLT: a slow local bus (80 MB/s) and fast direct data links (240 MB/s per Comp-FPGA). The hardware of the crate is connected by a standard Apache-server on the PMC as bridge to the outside world. Due to this standard interface, it is easy to change the software connection to possible upcoming new demands of the DAQ. Updates of the hardware could be easily integrated into the Apache-server. The overall programming layer is based on MATLAB containing the Graphical User Interface, parameterization of the hardware, control of the system and supervision of the measurements.

### 2.1.3. Aperture and patient bed

The aperture is formed by the transducers in a semi-elliptical TAS holder. The TAS holder acts also as the container for the contact medium water and has several openings for water supply and drainage. To accomplish the required accuracy, the TAS holder was manufactured by a CNC lathe from a solid poly-oxy-methylene (POM) block. The semi-elliptical aperture has a diameter of 26 cm and a height of 18 cm.

The whole device is embedded in a patient bed as shown in Fig. 1 with a length of 2 m, a width of 70 cm and a height of 90 cm. It holds the aperture connected to the data acquisition hardware, translation- and rotation mechanics and motors, power supplies, water reservoir and heating, and disinfection system. It is covered by a mattress and serves as examination couch.

### 2.1.4. Sparse aperture approach

A 3D system requires to fulfil sampling theorem a large number of transducers approx. two orders of magnitude more than a 2D system. The technical feasibility limits the number of transducer positions resulting in a sparse aperture and causing artefacts due to grating lobe effects in the resulting images [11].

For systems where the imaged object is in a defined region of interest (ROI), the sampling can be reduced to a number of transducers which guarantees non-sparse sampling within the ROI. For a linear array the distance between transducer elements should be smaller than  $0.5\lambda$  to prevent grating lobe artefacts [12]. A ring aperture requires a transducer distance smaller than  $0.5\lambda R/r$ , where  $R$  is the radius of the ring and  $r$  the radius of the ROI [13]. A semi-spherical aperture leads to an upper limit of

**Table 2**

Number of transducer  $N_{tr}$  for Nyquist sampling.

Geometry	R m	r mm	$\lambda$ mm	$N_{tr}$	Positions	Data GByte
Ring	0.115	50	0.8	785	40	103
Semi-sphere	0.1	12	0.75	$10^4$	1	130
	0.115	50	0.8	$1.2 \cdot 10^5$	1	43000

$(2\pi r/\lambda)^2$  transducers [14,15], if a uniform 1D sampling for the azimuth and elevation angles is applied. This results in an inhomogeneous 2D sampling of the aperture, as the sensor density at the poles of the sphere is very high. For an equiangular distribution of the transducer we could reduce the number of transducer by 20% (Table 2).

The limitation to a certain ROI with a small radius  $r$  explains at least partly the much smaller number of transducers for a spherical array reported by other authors in simulations: Norton and Linzer [16] consider 10 000 elements on a hemisphere, see Table 2, which fits quite well with the 10 107 transducers predicted from Driscolls and Healys [14] as upper limit. Grating lobe artefacts will only arise outside the simulated small volumes.

For an exemplary ring system with radius 11.5 cm (see Table 2) 103 GByte of raw data per breast have to be processed. To record, store and process this data is certainly challenging but feasible today.

For a fully sampled semi-sphere of this size (see Table 2) the number of transducers and the amount of data to be processed is no longer feasible. Therefore, a compromise between the number of transducers and the image quality has to be made, i.e. contrast between image content and grating lobe artefacts. A quantification of the signal-to-artefact ratio for the KIT 3D USCT can be found in [11].

## 2.2. Signal preprocessing and image reconstruction

### 2.2.1. Reflectivity reconstruction

The applied reconstruction algorithm for reflectivity images is the 3D synthetic aperture focusing technique (SAFT), which can be described by the following equation:

$$R(\vec{p}) = \sum_{j,k} \hat{a}(\vec{p}, \vec{e}_j, \vec{r}_k) T(A_{j,k}(t(\vec{p}))) \quad (1)$$

where  $R$  denotes the reconstructed qualitative volume of local impedance-differences,  $\vec{p}$  the reconstructed point,  $T$  contains the pre-processing steps,  $A_{j,k}$  is the A-scan acquired at emitting position  $\vec{e}_j$  and receiving position  $\vec{r}_k$ . The equation is valid for small attenuation, weak point scatterers, and spherical emittance. SAFT calculates at each image point the mean of all reflections which might originate from this position. Norton and Linzer [16] showed that for ideal conditions, i.e. continuous aperture, isotropic point scatterers and no attenuation, SAFT solves the inverse problem of calculating the local impedance differences.

The time  $t$  is related to the point  $\vec{p}$  by:

$$t(\vec{p}) = \frac{\|\vec{p} - \vec{e}_j\| + \|\vec{p} - \vec{r}_k\|}{\hat{c}(\vec{p}, \vec{e}_j, \vec{r}_k)}. \quad (2)$$

For the simplest reconstruction, the harmonic mean of the speed of sound may be assumed to be constant  $\hat{c}(\vec{p}, \vec{e}_j, \vec{r}_k) = c_0$ , e.g. the speed of sound of water at the temperature measured during image acquisition. Alternatively, more accurate estimations of the speed of sound distributions, e.g. a speed of sound map calculated from the recorded transmissions, can be applied. The factor  $\hat{a}(\vec{p}, \vec{e}_j, \vec{r}_k)$  is applied to correct for the attenuation on the path estimated from the attenuation map of the breast [17].

Acquiring unfocused ultrasound facilitates new possibilities for signal preprocessing, as the data can be accessed before the focus of emission is generated [18]. Here the preprocessing of the A-scans consists of three steps: First, a matched filter is applied to increase the signal-to-noise ratio, by correlating the signal with the known pulse shape and to apply pulse compression. This is followed by an envelope transformation and detection of the local maxima. To cope with the phase aberrations the resulting signal is convoluted by a pulse with an adapted lower bandwidth.

In summary, the preprocessing is:

$$T(A(t)) = \text{locMax}(|H(A(t) * p(t))|) \otimes p_{\text{opt}, \tau_{\text{new}}}(t) \quad (3)$$

where  $\text{locMax}$  denotes the local maximum,  $H$  the Hilbert transform,  $*$  the cross-correlation operator,  $p(t)$  the known pulse form, and  $\otimes$  the convolution operator.

The optimal pulse  $p_{\text{opt}, \tau_{\text{new}}}(t)$  for reflectivity imaging was introduced by Norton and Linzer [16] with

$$p_{\text{opt}, \tau_{\text{new}}}(t) = \frac{2\sqrt{\pi}}{\tau_{\text{new}}} \left[ 1 - 2 \left( \frac{\pi \cdot t}{\tau_{\text{new}}} \right)^2 \right] e^{-\left( \frac{\pi \cdot t}{\tau_{\text{new}}} \right)^2}, \quad (4)$$

where  $\tau_{\text{new}}$  is the new pulse duration, i.e. the main lobe of the optimum pulse. The main lobe of the optimal pulse was set to 2  $\mu\text{s}$ , which corresponds to a Full Width Half Maximum (FWHM) of the point spread function of approx. 1.5 mm, and thus is comparable to MRI.

### 2.2.2. Transmission reconstruction

The speed of sound and attenuation are reconstructed using a ray-based approach. The transmission signals are detected and the time-of-flight and relative signal energy are applied to an algebraic reconstruction technique (ART) to calculate the resulting images. A compressive sensing algorithm, i.e. a 3D adaption of total variation minimization (TVAL3) is employed for optimization. Refer to [19] for a more detailed description.

### 2.2.3. Speed-up

The computing system for reconstruction consists of a PC (4  $\times$  AMD Opteron Octacore, 2.3 GHz, 256 GB RAM) and an external crate for Graphical Processor Units (GPU) from One Stop Systems is connected via a second-generation PCI-Express bus. The external

GPU crate is equipped with four Nvidia Geforce GTX 590 cards, with two GF100 GPUs per card. This results in a total number of eight separate GPUs for image reconstruction [20].

### 2.2.4. Image fusion

The resulting reflectivity, speed of sound and attenuation images can be viewed separately, directly overlaid or overlaid with an applied threshold. The direct overlay codes the speed of sound or attenuation in a colour map and the reflectivity as grey values. The overlay is done by adding the colour-coded image to the grey image with an adjustable degree of transparency. The thresholded-fused image follows the method in [6], where a colour image only marks image areas where the speed of sound and attenuation are above given thresholds, and then is overlaid on top of the reflectivity volume.

## 3. Experimental evaluation of imaging properties

### 3.1. 3D PSF estimated from bonding wires

The predicted performance of the system, i.e. low spatial variance and isotropy of the 3D PSF, was evaluated in terms of FWHM: A bonding wire with a diameter of 0.07 mm, i.e. much thinner than the theoretical resolution of the system, was manually twisted into a helical structure within a bounding box of 5.2 cm  $\times$  4.3 cm  $\times$  6.5 cm, so that the FWHM could be measured from many directions.

The 2D FWHM profile was measured at 40 spatially distributed evaluation points. First, a small volume around each evaluation point was cut out, smaller than the local bending of the twisted wire so that the cut could be approximated by a cylinder. The detailed procedure is described in [21].

The wire was imaged with fourfold averaging and 887 364 emitting-receiving combinations, i.e. one aperture position. A pulse with centre frequency of 2.4 MHz and 2 MHz bandwidth was applied for excitation of the emitters. The applied optimal pulse in the preprocessing had a pulse duration of  $\tau_{\text{new}} = 0.35 \mu\text{s}$ . The so prepared A-scans were used for ellipsoidal back-projection into the volume. The voxel size of the reconstructed volume was  $(0.06 \text{ mm})^3$ . Fig. 2 shows a photo of the twisted wire and the reconstructed 2D profiles in 3D.

Firstly, the standard deviation of the mean FWHM of the 40 evaluated points was measured to 36  $\mu\text{m}$  (predicted: 35  $\mu\text{m}$ ).

Secondly, to evaluate the isotropy of the system's point spread function in 3D a global 3D PSF was estimated by fitting an ellipsoid to the 2D FWHM profiles centred at zero, after evaluation of an approx. uniform angular distribution of the normal of the planes containing the 2D FWHM profiles. The fitted ellipsoid had nearly isotropic diameters of  $d_{x,y,z} = (0.2, 0.26, 0.24) \text{ mm}$ , (predicted:  $(0.2, 0.2, 0.25) \text{ mm}$ ).

Thirdly, the overall mean of the measured FWHMs was calculated to  $0.24 \text{ mm} \pm 0.05 \text{ mm}$  as measure of the resolution of the system (predicted: 0.22 mm).

To achieve this resolution in the reflection images in the range of  $\frac{\lambda}{2}$  for complex objects, the reconstruction algorithm has to include the speed of sound distribution measured in transmission tomography, see Eq. (2).

### 3.2. Clinical value of transmission tomography

Speed of sound and attenuation are new modalities to differentiate between different tissue types as proposed by Greenleaf [9]. In order to estimate the clinical value of sound speed and attenuation we used 2D data of the Karmanos group's USCT system [22]. As ground truth for visible tissue types corresponding X-ray mammograms of the same patient were used. They were



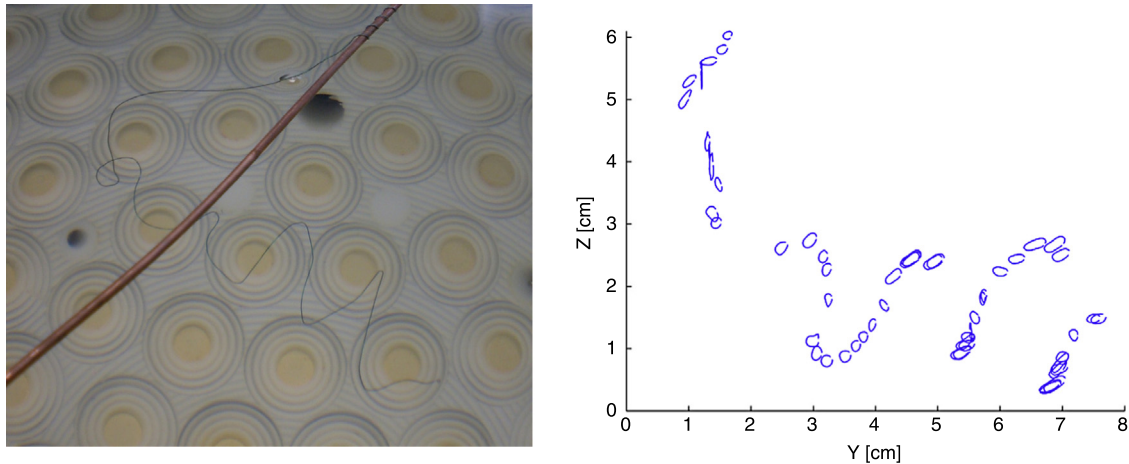


**Fig. 2.** Bonding wire for PSF assessment. Left: photo. Right: 2D profiles at the evaluation points and their direction and position in space. Scaled up to a factor 3 for better visibility.

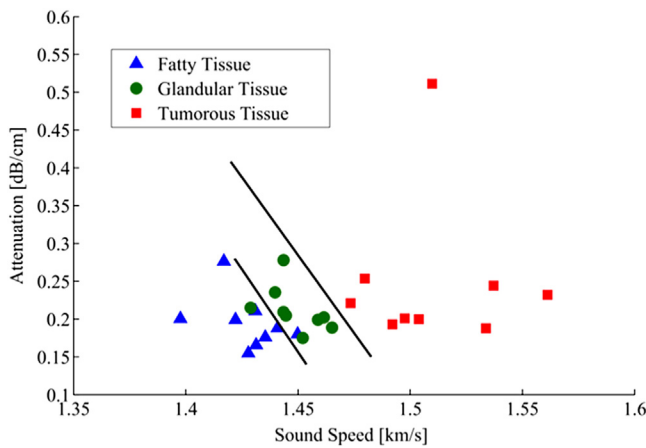


**Fig. 3.** In collaboration with the Karmanos group [22] classification of different tissue types of the breast in 9 patients by transmission tomography. The black lines represent thresholds computed by a linear support vector machine to separate fatty from glandular tissue and glandular from tumour tissue.

segmented into three tissue classes: fatty, fibro-glandular and tumour tissue. An image registration was applied to align every pixel of the X-ray mammogram with a pixel of a maximum intensity projection of the USCT sound speed and attenuation volume. For each tissue class in the X-ray mammogram, the corresponding mean sound speed and attenuation value were extracted by averaging over the pixels of the corresponding pixel region in the sound speed and attenuation map. Fig. 3 shows the results of the evaluation with 9 patients: by sound speed and attenuation we were able to separate fatty, fibro-glandular and tumour tissue very well. To calculate thresholds for the tissue classes, a linear support vector machine classifier was applied leading to the black lines depicted in Fig. 3. For all 9 patients the tumour could be well separated from healthy tissue. The inclination of the separating lines may be an indication for the effect of embedded connective tissue on speed of sound and attenuation, but this has to be researched further.

#### 4. First clinical study

The primary aim of the clinical study was to test the USCT device on ten patients in respect to

- (1) Data acquisition and image reconstruction protocols.
- (2) Fused display of the multimodal USCT images.

**Table 3**

Breast dimensions in the pilot study.

Mean (STD) (in mm)	X direction	Y direction	Z direction
MRI	112 (22)	114 (13)	80 (19)
USCT	151 (25)	143 (16)	66 (13)
Difference	35%	25%	−17%

(3) Process of data acquisition and its optimization.

#### 4.1. Sequence of imaging a patient

The patients included in the study were acquired during the standard MRI examination at the University Hospital Jena. They first had their scheduled MRI examination and were then-if they met the inclusion criteria - asked to participate in the study. If they agreed, the USCT image acquisition was carried out directly after the MRI, so that the MRI images could be used as ground truth for comparison to the USCT volumes.

The patient was asked to disinfect her breasts. Then she laid on the patient mattress and positioned the first breast into the USCT device. The central positioning of the breast was monitored and corrected using a B-scan like preview. Then the data acquisition for this breast was started. The same process was, if applicable, repeated for the second breast. At the end the patient was asked to fill a questionnaire to rate the imaging procedure. Before the next patient was examined, the data was read out onto a hard disc, the water was exchanged and the device disinfected.

#### 4.2. Imaging parameters

For emission a linear frequency coded chirp with 2.5 MHz centre frequency, 1 MHz bandwidth and 12.8  $\mu$ s duration was employed. Patients with breast lesions were imaged with ten aperture positions. For two patients, who were diagnosed with large cancer masses, the breasts with lesions were imaged with 13 aperture positions.

#### 4.3. MRI as ground truth

In all MRI examinations a standardized protocol according to international guidelines was used. The applied magnetic field strength was 1.5 T (Magnetom Avanto; Siemens Medical, Erlangen, Germany). It started with scans of 2D dynamic T1w spoilt gradient

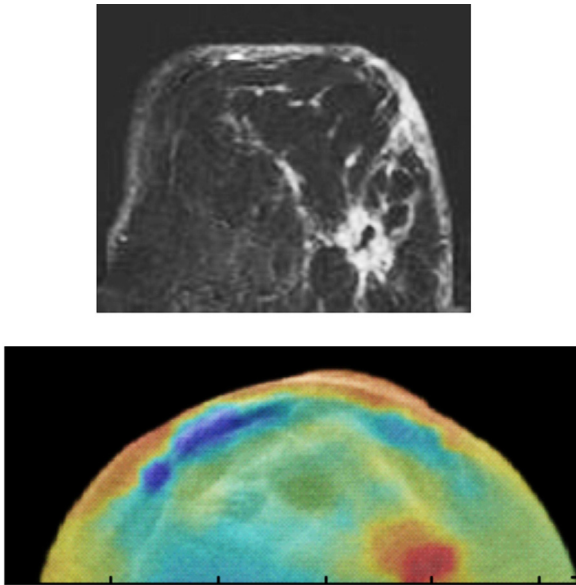


**Fig. 4.** 64 year old patient with a large breast cancer in the left breast. Top image: Transversal MRI subtraction slice. Bottom image: Speed of sound overlaid on top of reflectivity slice at approx. the same position.

echo protocol before and after intravenous application of the contrast agent Gd-DTPA (Magnevist, Bayer/Schering, Leverkusen, Germany). For standardized injection a device from (Medrad, Spectris, Medrad, Pittsburgh, USA) was used. Additionally, a T2w TSE scan using a 2D dynamic protocol in identical slice position was acquired. The MRIs are sliced transversally, the in-plane resolution was 0.9 mm, and the slice thickness was 3 mm without gap.

#### 4.4. Patients statistics and breast sizes

The average age of the ten patients was 55.6 years ( $\pm 13.5$  years). The youngest patient was 37 years and the oldest 78 years.

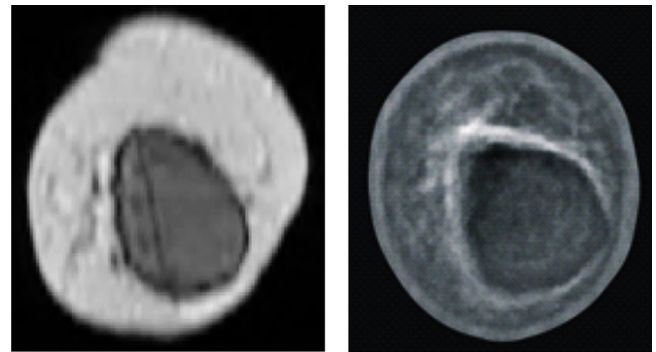
The breast shape in MRI and USCT are expected to differ in spite of similar patient positioning in prone position, because the water bath in the USCT gives rise to buoyancy of the breast. To evaluate this, the breasts dimensions in the MRI and USCT were manually measured in  $x$ ,  $y$ ,  $z$  (mediolateral, craniocaudal, anteroposterior) direction from the images. To match the amount of breast imaged in the different devices, the  $z$  dimension in the MRI was estimated by correlating structures visible in the last slices of the USCT volume to the MRI structures. Any rotations or deformations were ignored.

Table 3 shows the mean and standard deviation of the 18 breasts' dimensions. Due to the buoyancy, the breasts were in average broader in the USCT compared to the MRI but shortened in the  $z$  direction.

#### 4.5. Problems: patient positioning and breast deformation

The breasts in the USCT volumes were partly shorter in  $z$  dimension than expected, even when taking the buoyancy effect into account. It seems some of the patients did not fully immerse the breast into the water bath. To overcome this problem, we improved the construction of the patient bed.

Direct voxel to voxel comparisons between the MRI and the USCT volume were not possible due to differences in patient positioning. In the MRI the larger breasts were deformed by the mamma coil of the MRI, which led to a nonlinear deformation with a non-central nipple position in the MRI, see e.g. transversal MRI slice in Fig. 4.



**Fig. 5.** 58-year-old patient with a breast implant (right breast). Left: Frontal MRI T1 slice. Right: USCT slice at approx. same position.

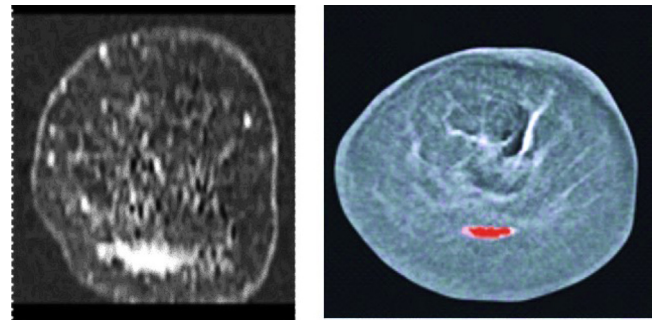


**Fig. 6.** 74-year-old patient with large breast cancer (left breast). Left: Frontal MRI subtraction slice. Right: USCT slice at approx. the same position.

#### 4.6. Timelines

During the pilot study we could image approximately one patient per hour, which fitted quite well into the clinical process. For preparation of the device and patient information we needed between 15 and 30 min. The patient positioning took approx. 2 to 5 min per breast and the image acquisition in sum 11 min. In the meantime, the data was read out (14 min), the device was disinfected and the water was exchanged, sterilized and heated (approx. 15 min).

The data acquisition time is mainly dominated by the time to move the aperture between different aperture positions. This time is depending on the path to be travelled. The mean time for DAQ with one movement during the pilot study was 50 s. In the meantime patient positioning and aperture movement could be accelerated by a factor two. Patient movement ( $< 1$  mm [23]) could be corrected due to multiple sampling used.

The SAFT reconstructions took approx. 6.2 h per breast volume including speed of sound and attenuation correction for data acquired at ten aperture positions. Now with a GPU implementation this time is reduced to 20 min. The volumes were gamma corrected before display. The transmission reconstruction took about 15 min per breast per modality without the use of GPUs.

#### 4.7. Clinical Results

Fig. 4 shows a patient with a large breast cancer in left breast. The top image shows a transversal MRI subtraction slice with the cancer highlighted by contrast agent at the right bottom corner. The lower image shows an overlaid USCT slice at approx. the same position, highlighting the area which is comparable to the cancer position in the MRI by a high speed of sound. The patient had a D-cup, the diameter of the breast displayed in the MRI slice is

13 cm and in the USCT slice 18 cm due to buoyancy.

Fig. 5 displays a patient with a breast implant in the right breast. The left image shows a frontal slice of the native T1 MRI. The right image shows a reflectivity slice at approx. the same position. The breast had a diameter of approx. 8.7 cm in both images.

Fig. 6 shows in the left image a frontal MRI subtraction slice, which was interpolated to fit the in-plane resolution. The large cancer is highlighted by a Gd contrast agent. The right image shows a thresholded-fused USCT slice at approx. the same position, highlighting a high speed of sound and attenuation area which is comparable to the cancer position in the MRI.

## 5. Discussion and conclusion

We developed an optimized, unfocused 3D USCT with approximately isotropic 3D PSF and presented first images which demonstrate the performance of the system. We realized a sparse 3D USCT setup, resulting in homogeneous illumination, and nearly isotropic 3D PSF.

Image reconstructions with a wire and a clinical phantom confirm this: Currently, the mean FWHM in three dimensions is 0.24 mm with low dimensional and spatial deviation. The contrast of the reconstructed 3D volume of a breast phantom is very satisfactory in spite of our sparse aperture. The resolution is comparable to the high-quality MRI volume.

It seems that speed of sound is at the current state the most indicating modality for cancer. The spatial resolution of speed of sound and attenuation is currently limited by the ray based reconstruction algorithm in the range of 5 to 12 mm. Yet, this needs further evaluation. More complex reconstruction methods for transmission tomography leading to higher resolution are under test.

Patient positioning is crucial for imaging with our system. Displacements in the (transversal)  $x - y$  plane cause the illumination of the breast to vary strongly. Displacement in  $z$  (anterior-posterior) direction leads to suboptimal coverage of the breast; the proximal part of the breast is then not imaged. Patient movement seems to be a minor problem; no definite movements between reconstructions of the single aperture positions could be detected. Breathing movement of the patients seems to have no effect on the images of the breast. The duration of the now improved data acquisition to 6 min per breast seemed to be acceptable for the patients. The process of breast examination with USCT was described as relatively comfortable by the patients.

The next step in this work is to carry out a large clinical study and build a new 3D USCT system with higher contrast for reflection and position resolution for transmission tomography, a factor 4 shorter data acquisition time and a better access to the chest. Faster reconstruction time will additionally be given by Moore's law.

## References

- [1] H. Schomberg, An improved approach to reconstructive ultrasound tomography, *J. Phys. D: Appl. Phys.* 11 (1978).
- [2] M. Nguyen, H. Bressmer, et al., Improvements in ultrasound transmission computed tomography, *Proc. European Conference on Engineering and Medicine* (1993) 189190.
- [3] M. Ashfaq, H. Ermert, A new approach towards ultrasonic transmission tomography with a standard ultrasound system, *Proc. IEEE UFFC Symp.* 3 (2004) 184851.
- [4] S. Mensah, P. Lasaygues, E. Debieu, E. Franceschini, ANAIS: an ultrasound mammograph, *J. Acoust. Soc. Am.* 123 (5) (2008) 30023002.
- [5] R. Stotzka, J. Würfel, T.O. Müller, H. Gemmeke, Medical imaging by ultrasound computer tomography, *Proc. SPIE Med. Imag.* (2002) 110–119.
- [6] N. Duric, P. Littrup, P. Chandiwal-Mody, C. Li, S. Schmidt, L. Myc, O. Rama, L. Bey-Knight, J. Lupinacci, B. Ranger, A. Szczepanski, E. West, In-vivo imaging results with ultrasound tomography: report on an ongoing study at the karmanos cancer institute, *Proc. SPIE Med. Imag.* 7629 (2010) 76290M.
- [7] J. Wiskin, D. Borup, S. Johnson, M. Berggren, D. Robinson, J. Smith, J. Chen, Y. Parisky, J. Klock, Inverse scattering and refraction corrected reflection for breast cancer imaging, *Proc. SPIE Med. Imag.* 7629 (2010) 76290K.
- [8] G. Schwarzenberg, M. Zapf, N.V. Ruiter, Aperture optimization for 3D ultrasound computer tomography, *Proc. IEEE UFFC Symp.* (2007) 1820–1823.
- [9] J.F. Greenleaf, R.C. Bahn, Clinical imaging with transmissive ultrasonic computerized tomography, *IEEE Trans. Biomed. Eng.* 28 (2) (1981) 177–185.
- [10] A. Kopmann, T. Bergmann, H. Gemmeke, M. Howe, M. Kleifges, A. Menshikov, D. Tcherniakhovski, J.F. Wilkerson, S. Wuestling, FPGA-based DAQ system for multi-channel detectors, *Proc. IEEE NSS MIC* (2008).
- [11] N.V. Ruiter, M. Zapf, T. Hopp, H. Gemmeke, Experimental evaluation of noise generated by grating lobes for a sparse 3D ultrasound computer tomography system, *Proc. SPIE Med. Imaging* (2013).
- [12] M. Lang, H. Ermert, Linear synthetic aperture modes for ultrasonic pulse-echo imaging, *Biomedizinische Technik* 42 (5) (1997).
- [13] F. Simonetti, L. Huang, N. Duric, On the sampling of wave fields with circular ring apertures, *J. Appl. Phys.* 101 (2007).
- [14] J.R. Driscoll, D.H. Healy, Computing fourier transforms and convolutions on the 2-sphere, *Advances in Applied Mathematics* 15 (1994).
- [15] F. Simonetti, L. Huang, Synthetic aperture diffraction tomography for three-dimensional imaging, *Proc. R. Soc. Lond. Ser. A Math. Phys. Eng. Sci.* 465 (2009).
- [16] S. Norton, M. Linzer, Ultrasonic reflectivity imaging in three dimensions: Reconstruction with a spherical array, *Ultrasonic Imaging* 1 (3) (1979) 21031.
- [17] E. Kretzek, R. Dapp, M. Zapf, M. Birk, N.V. Ruiter, Evaluation of phase aberration correction for a 3D USCT using a ray trace based simulation, *Proc. IEEE UFFC Symp.* (2013) 378–381.
- [18] N.V. Ruiter, G.F. Schwarzenberg, M. Zapf, H. Gemmeke, Improvement of 3D ultrasound computer tomography images by signal pre-processing, *Proc. IEEE UFFC Symp.* (2008) 852–855.
- [19] R. Dapp, M. Zapf, N.V. Ruiter, et al., Geometry Independent Speed of Sound Reconstruction for 3D USCT Using Apriori Information, *Proc. IEEE UFFC Symp.* (2011) 1403–1406.
- [20] E. Kretzek, M. Zapf, M. Birk, H. Gemmeke, N.V. Ruiter, GPU based acceleration of 3D USCT image reconstruction with efficient integration into MATLAB, *Proc. SPIE Med. Imag.* 8675 (2013) 867500.
- [21] N.V. Ruiter, M. Zapf, H. Gemmeke, Evaluation of 3D point spread function of a semi-ellipsoidal ultrasound computer tomography system, *Proc. IEEE UFFC Symp.* (2011).
- [22] T. Hopp, A. Stromboni, N. Duric, N.V. Ruiter, Evaluation of breast tissue characterization by ultrasound computer tomography using a 2D/3D image registration with mammograms, *IEEE Ultrasonics Symp.* (2013).
- [23] N.V. Ruiter, T. Hopp, M. Zapf, E. Kretzek, H. Gemmeke, Analysis of patient movement during 3D USCT data acquisition, *Proc. SPIE Med. Imag.* 9790 (2016) 97900A.